This is an open access article published under a Creative Commons Attribution (CC-BY) License, which permits unrestricted use, distribution and reproduction in any medium, provided the author and source are cited.

ACS AUTHORCHOICE

JACS
JOURNAL OF THE AMERICAN CHEMICAL SOCIETY

pubs.acs.org/JACS

Article

Halide Perovskite–Lead Chalcohalide Nanocrystal Heterostructures

Muhammad Imran,[▽] Lucheng Peng,[▽] Andrea Pianetti, Valerio Pinchetti, Julien Ramade, Juliette Zito, Francesco Di Stasio, Joka Buha, Stefano Toso, Jun Song,* Ivan Infante,* Sara Bals,* Sergio Brovelli,* and Liberato Manna*

Cite This: *J. Am. Chem. Soc.* 2021, 143, 1435–1446

Read Online

ACCESS | Metrics & More | Article Recommendations | Supporting Information

ABSTRACT: We report the synthesis of colloidal $CsPbX_3$–$Pb_4S_3Br_2$ (X = Cl, Br, I) nanocrystal heterostructures, providing an example of a sharp and atomically resolved epitaxial interface between a metal halide perovskite and a non-perovskite lattice. The $CsPbBr_3$–$Pb_4S_3Br_2$ nanocrystals are prepared by a two-step direct synthesis using preformed subnanometer $CsPbBr_3$ clusters. Density functional theory calculations indicate the creation of a quasi-type II alignment at the heterointerface as well as the formation of localized trap states, promoting ultrafast separation of photogenerated excitons and carrier trapping, as confirmed by spectroscopic experiments. Postsynthesis reaction with either Cl^- or I^- ions delivers the corresponding $CsPbCl_3$–$Pb_4S_3Br_2$ and $CsPbI_3$–$Pb_4S_3Br_2$ heterostructures, thus enabling anion exchange only in the perovskite domain. An increased structural rigidity is conferred to the perovskite lattice when it is interfaced with the chalcohalide lattice. This is attested by the improved stability of the metastable γ phase (or "black" phase) of $CsPbI_3$ in the $CsPbI_3$–$Pb_4S_3Br_2$ heterostructure.

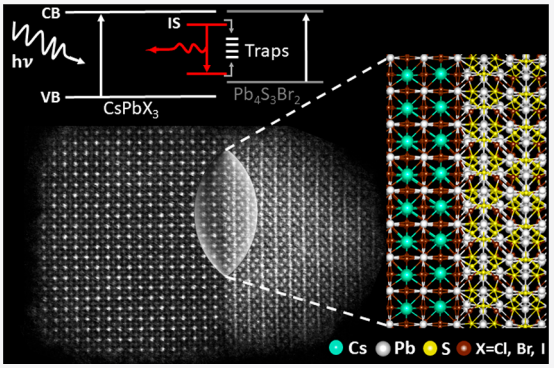

INTRODUCTION

Metal halide perovskites and especially $CsPbX_3$ (X = Cl, Br, I) in the form of colloidal nanocrystals (NCs) have witnessed a rapid development in the past few years due to their ease of processing, tunable band gaps, narrow emission line width, and defect-tolerant nature, all features that make them appealing for optoelectronic devices.[1−11] Also, various groups have tackled the synthesis of NC heterostructures in which the perovskite domain is bound to a domain of another material.[12,13] Examples include metal–perovskite (Au–$CsPbBr_3$),[14] metal chalcogenide–perovskite (PbS–$CsPbX_3$,[15] ZnS–$CsPbX_3$,[16,17] and PbSe–$CsPbX_3$[18]), metal dichalcogenide–perovskite (Cs_2SnI_6/SnS_2),[19] $CsPbX_3$/metal oxide Janus (TiO_2–$CsPbBr_3$,[20] $CsPbX_3$/SiO_2,[21] $CsPbX_3$/ZrO_2,[22] and $CsPbBr_3$/TiO_2[23]), CsBr–$CsPbBr_3$,[24] and Cs_4PbBr_6–$CsPbBr_3$ NCs.[25] The latter case is a particularly revealing example of an epitaxial heterointerface (recently disclosed by our group), in which it is possible to observe a continuity of the sublattice of Cs^+ cations across the interface between the two domains, a common theme underlying the various heterostructures involving metal halide NCs.[26] Many of these nano-heterostructures may find applications in various fields, such as solar cells, LEDs, and photocatalysis.[23,27,28]

In the present work, we report a new type of heterostructure, in which a halide perovskite NC shares an epitaxial interface with a lead chalcohalide NC. Colloidal NCs of lead chalcohalides have been recently synthesized in our group:[29] they are characterized by an indirect band gap, are nonemissive at room temperature, and are stable for months under ambient conditions.[29] The synthesis that we discuss in this work initially delivers $CsPbBr_3$–$Pb_4S_3Br_2$ NCs: from them, we could further prepare, by postsynthesis anion exchange, the corresponding heterostructures in which the perovskite domain is either $CsPbCl_3$ or $CsPbI_3$. In other words, anion exchange only affects the perovskite region and not the chalcohalide one, which remains $Pb_4S_3Br_2$. In all these heterostructures, the two domains are separated by a sharp interface. Epitaxial relationships between the two domains are possible due to a favorable matching of the respective Pb sublattices in the two structures, when they are arranged in some specific mutual orientations.

In all the systems studied, density functional theory (DFT) calculations highlight that the interface joining $CsPbX_3$ and $Pb_4S_3Br_2$ leads to a significant change in the electronic structures of the individual components. In the heterostructure, the edge of the valence band is localized almost completely in the chalcohalide domain, whereas the edge of the conduction band is distributed almost evenly across the

Received: October 17, 2020
Published: January 13, 2021

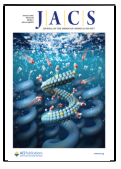

Downloaded via 107.178.203.199 on April 1, 2024 at 10:47:52 (UTC).
See https://pubs.acs.org/sharingguidelines for options on how to legitimately share published articles.

© 2021 American Chemical Society

https://dx.doi.org/10.1021/jacs.0c10916
J. Am. Chem. Soc. 2021, 143, 1435–1446

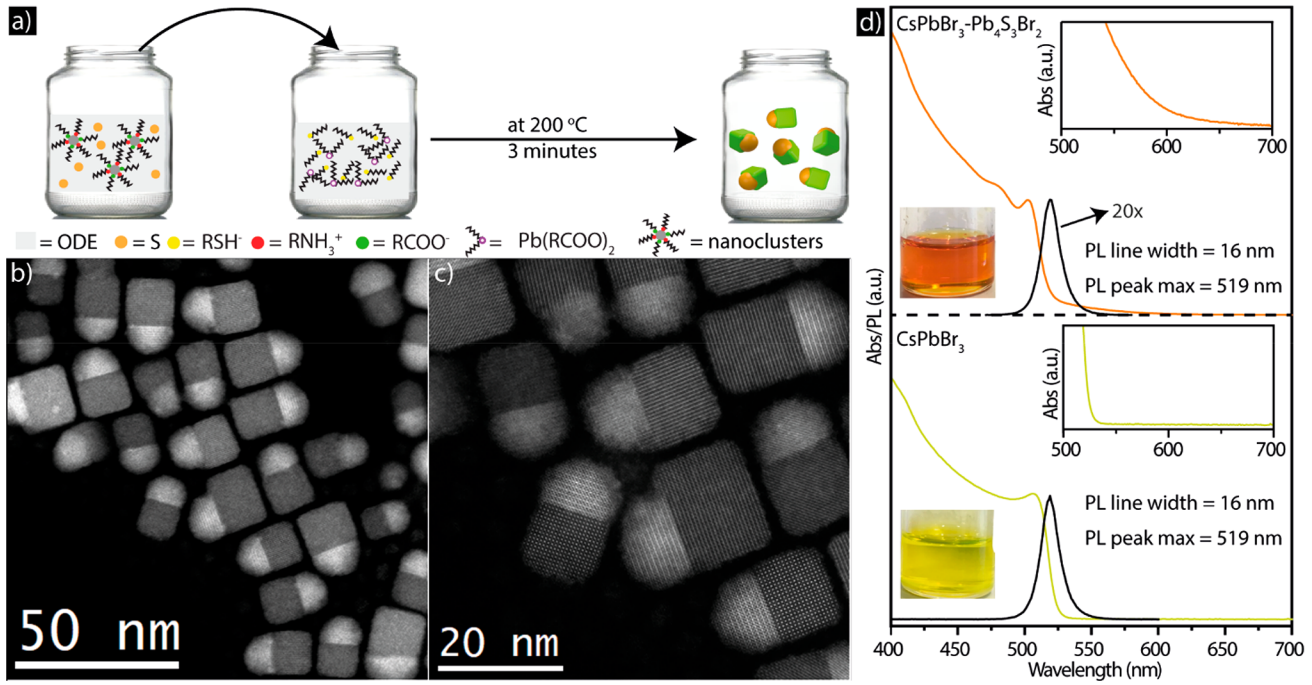

Figure 1. (a) Sketch describing the synthesis of the $CsPbBr_3$−$Pb_4S_3Br_2$ heterostructures. STEM images of (b, c) $CsPbBr_3$−$Pb_4S_3Br_2$ NCs at two different magnifications. (d) Absorbance and PL spectra of dispersions in toluene of the $CsPbBr_3$−$Pb_4S_3Br_2$ heterostructures and the $CsPbBr_3$ NCs, along with the photographs of the corresponding colloidal dispersions under room light. The insets are magnified absorption features in the 500−700 nm range for both samples.

heterostructure. This indicates that the overall system is not just the sum of its components but a potentially valuable platform for wave function engineering strategies that are not typically accessible with halide perovskite materials due to compositional alloying promoted by ion migration. The resulting quasi-type II-like energy level alignment at the heterojunction promotes the rapid splitting of photogenerated excitons with the photoexcited hole localized in the chalcohalide domain and the electron partially delocalized in the entire nanostructure. This, together with the rapid carrier trapping at interface localized states, as also predicted by DFT, leads to a nearly complete suppression of the photoluminescence (PL) with respect to the pure NCs. Nonetheless, low-temperature spectroscopic measurements reveal a red-shifted PL (compared to that from pure $Pb_4S_3Br_2$ NCs), which is likely due to the optical recombination of interface trapped carriers, whose efficiency is substantially affected by non-radiative channels. Notably, the presence of the interface confers higher structural rigidity to the perovskite lattice. This is evident in the $CsPbI_3$−$Pb_4S_3Br_2$ heterostructure, in which the $CsPbI_3$ domain over time does not transform to the thermodynamically stable δ "yellow" phase, as is well established for $CsPbI_3$ NCs, but remains in the metastable "black" γ phase.

RESULTS AND DISCUSSION

Synthesis. The synthesis of the heterostructures started with the preparation and purification of $CsPbBr_3$ nanoclusters, following a previously reported method.[30] These clusters, of subnanometer size, have an exciton absorption at 402 nm and are nonemissive at room temperature (Figure S1). They have been recently prepared and used as convenient "monomers" for the growth of perovskite NCs, as they enable a more precise control over size and shape than by using a standard synthesis approach, including the possibility to access branched geometries.[31] In the preparation of these clusters, both oleic acid and oleylammine were used. It is therefore likely that their surface is coated by both oleate and oleylammonium ions. In a typical synthesis, these nanoclusters were mixed with a solution of elemental sulfur dissolved in degassed octadecene (ODE), and the resulting mixture was injected in a vial containing a solution of dodecanethiol and lead oleate in degassed ODE, heated at 200 °C (Figure 1a). The reaction was allowed to proceed for 3 min and was subsequently quenched by immersing the vial in an ice water bath. The NCs were collected by centrifugation and were then redispersed in toluene for further use (see the Experimental Section for further details).

High angle annular dark field scanning transmission electron microscopy (HAADF-STEM) analysis evidenced the presence of heterostructures formed by a cubic shaped domain bound to a more rounded and higher contrast domain with an edge length of 20.3 ± 2.2 nm, most often along one face of the cube (Figure 1b,c; see also the TEM images of Figures S2 and S3). A statistical analysis done on ∼1300 NCs of Figure S2 indicated that only around 80 NCs (i.e., around 6% of the total) were cubes, apparently not carrying an additional domain attached to them. On the other hand, contrast variations in most of these cubes suggest that most of them were heterostructures as well, but they were simply sitting on the substrate in a vertical (face up) or lateral projection (see the examples in Figures S4 and S5). Overall, we can state that the fraction of isolated $CsPbBr_3$ NCs in this sample was definitely below 6%. If instead the initial $CsPbBr_3$ nanoclusters were heated under the same conditions as in the synthesis that we have just described for the heterostructures of Figure 1b,c, but in ODE alone (that is, with no elemental sulfur, dodecanethiol, and lead oleate), the product was represented

https://dx.doi.org/10.1021/jacs.0c10916
J. Am. Chem. Soc. 2021, 143, 1435−1446

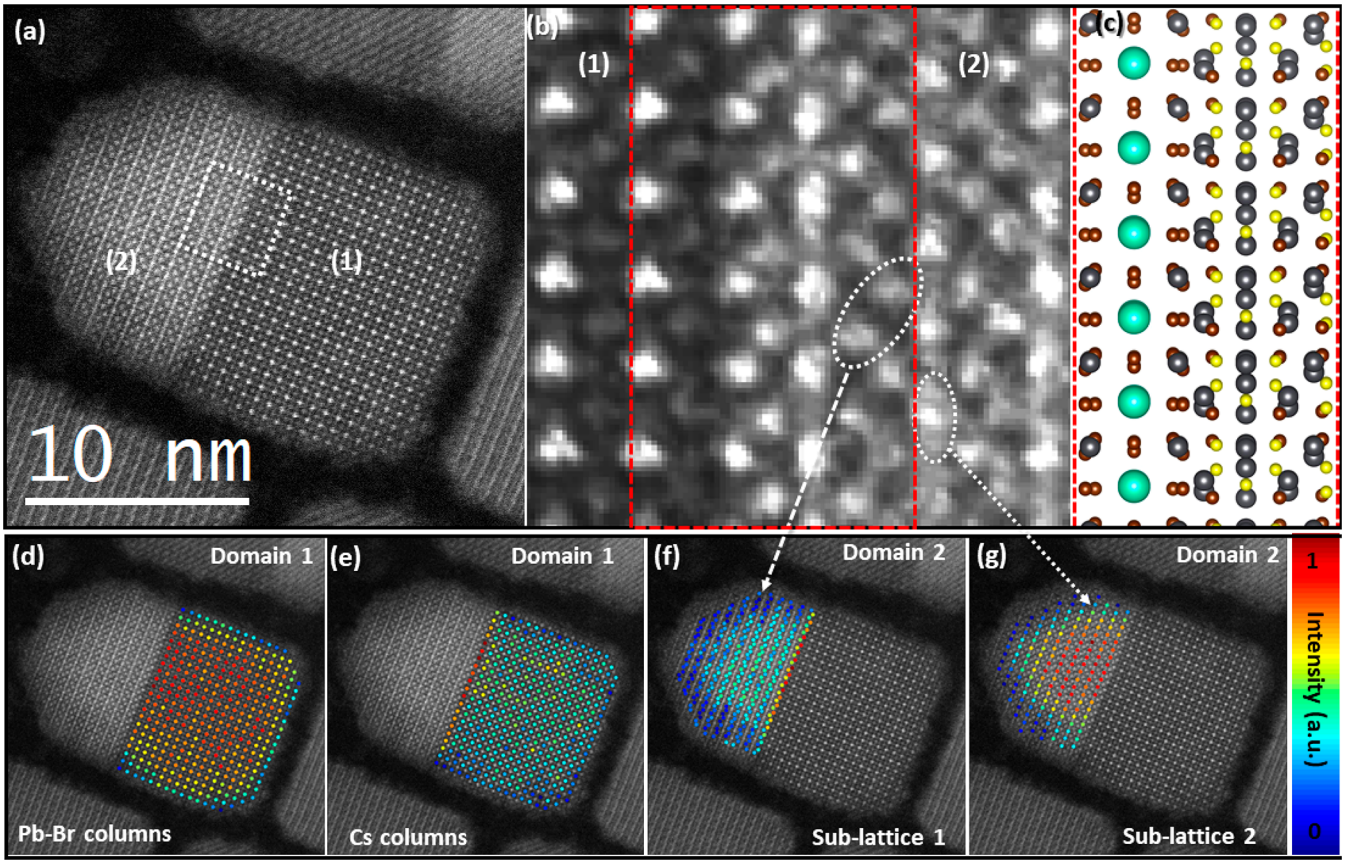

Figure 2. Structural analysis of a single $CsPbBr_3$–$Pb_4S_3Br_2$ heterostructure. (a) High-resolution HAADF-STEM image of a single heterostructure composed by a $CsPbBr_3$ (1) and a $Pb_4S_3Br_2$ (2) domains. (b) Magnified image of the region highlighted in white in (a), depicting the interface between $CsPbBr_3$ and $Pb_4S_3Br_2$ domains. The region highlighted in red represent a $Pb_4S_3Br_2$ pattern oriented along the [101] zone axis, as confirmed in (c) showing the $CsPbr_3$ and $Pb_4S_3Br_2$ structural model along this orientation. (d) Column intensity map of Pb–Br columns of the perovskite phase. (e) Column intensity map of Cs columns of the perovskite phase. (f) and (g) represent the intensity map of Pb columns belonging to the $Pb_4S_3Br_2$ domain.

by nearly monodisperse $CsPbBr_3$ cube-shaped NCs with an edge length of 15.9 ± 1.6 nm (Figure S6).

Optical absorption and photoluminescence (PL) spectra of colloidal dispersions of the cube-shaped $CsPbBr_3$ NCs and of the heterostructures are reported in Figure 1d. Compared to the $CsPbBr_3$ NCs, the heterostructures exhibited an additional absorption tail at long wavelengths, which became more prominent for wavelengths shorter than 550 nm. The two insets of Figure 1d are magnified views of the absorption features in the range 500–700 nm for both samples. For the heterostructure, this feature matched closely the optical absorption spectrum of our recently synthesized $Pb_4Br_3S_2$ NCs.[29] The $CsPbBr_3$ NCs evidenced the typical narrow PL peak (full-width-half-maximum, FWHM, of 16–17 nm) at 519 nm. The formation of the heterostructure led to a substantial suppression of the $CsPbBr_3$ NC emission, as discussed in detail later. The much weaker emission from the heterostructures sample (~5% of the $CsPbBr_3$ NC PL intensity) can be ascribed to the few $CsPbBr_3$ NCs present in solution that are not bound to a $Pb_4S_3Br_2$ domain, in quantitative agreement with the statistical analysis of the wide-field TEM images of Figure S2 (indicating less than ~6% residual $CsPbBr_3$ cubes).

The X-ray powder diffraction (XRPD) pattern of the cubes (Figure S7) contained diffraction features that are ascribable to the orthorhombic phase of $CsPbBr_3$. The pattern of the heterostructures had the same features as that of the $CsPbBr_3$ cubes, with additional peaks appearing around 25° and 36° (2θ). To identify the origin of these extra peaks, we recorded XRPD patterns of $Pb_4Br_3S_2$ NC and of mixtures of $CsPbBr_3$ and $Pb_4Br_3S_2$ NC powders (see Figure S8 for an overall comparison of the XRPD patterns of the various samples). A comparison of these various patterns confirmed that the XRPD pattern of the heterostructures had contribution from both phases, albeit with strong predominance of the signal from the perovskite domain.

We tested the influence of reaction temperature, time, relative concentrations of dodecanethiol and of lead oleate, and addition of oleylammonium bromide (OLAM-Br) on the formation of the heterostructures, while keeping the concentration of $CsPbBr_3$ clusters constant. Details on all these tests are reported in the Supporting Information (Figures S9–S15). In brief, the optimal temperature window for growing the heterostructures was around 200 °C. At sensibly lower temperatures (150 °C or below) no heterostructures were formed, and at higher temperatures (230 °C) the size and shape distributions worsened considerably (Figure S9). We then tested the influence of dodecanethiol in syntheses performed at the optimal temperature of 200 °C. In the absence of dodecanethiol (Figure S10a), no $CsPbBr_3$–$Pb_4S_3Br_2$ heterostructures were formed, and instead we obtained large $CsPbBr_3$ NCs, each carrying a tiny, low contrast domain attached to it. At increasing amounts of dodecanethiol

https://dx.doi.org/10.1021/jacs.0c10916
J. Am. Chem. Soc. 2021, 143, 1435–1446

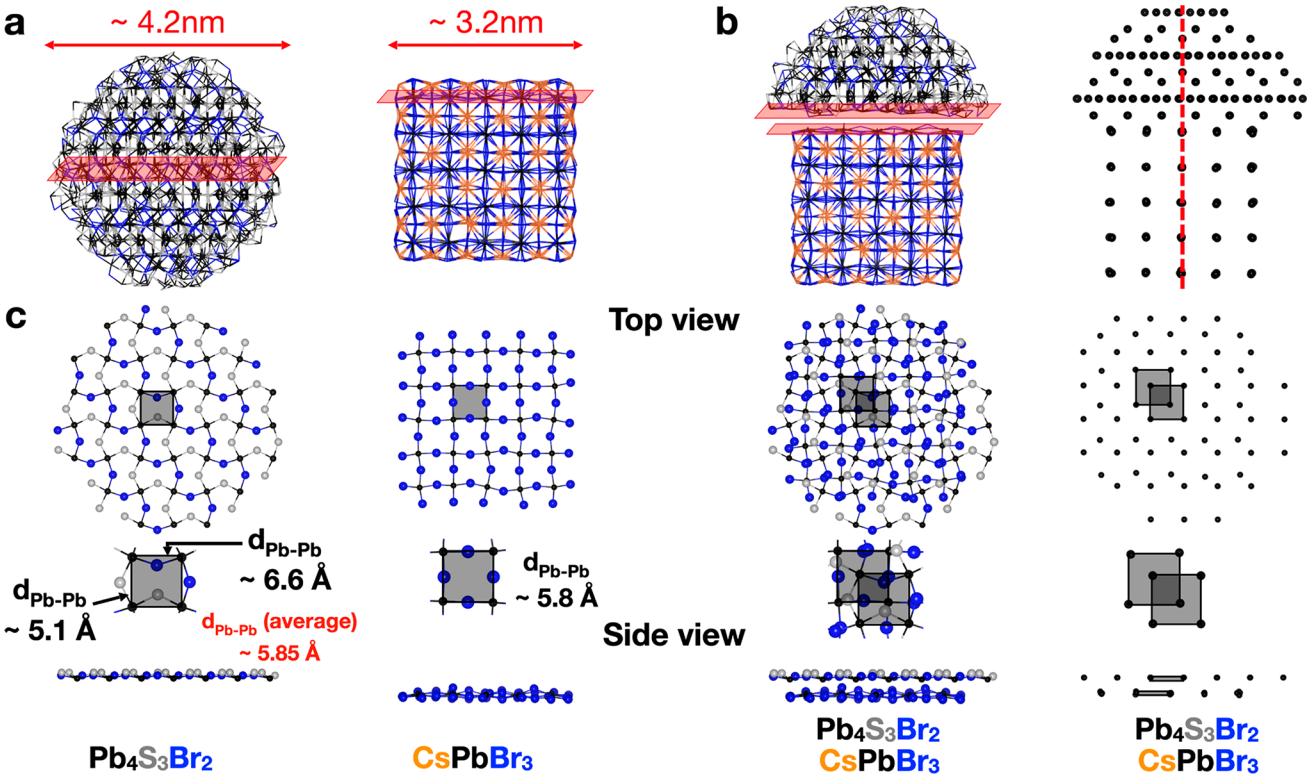

Figure 3. (a) Sticks representation of (left) a spherical ~4.2 nm diameter $Pb_{548}S_{423}Br_{250}$ NC model and (right) a cubic ~3.2 nm sided $Cs_{200}Pb_{125}Br_{450}$ NC model optimized at the DFT/PBE level of theory. (b) Preparation of the heterostructure NC model by (left) stacking of the $Pb_4S_3Br_2$ and $CsPbBr_3$ moieties and (right) alignment of their Pb ions along the [010] axis. (c) Top and side view of the interface layers of both the $Pb_4S_3Br_2$ and $CsPbBr_3$ nanocrystals. A cell of four Pb ions was taken to demonstrate the smooth alignment at the interface. The radial distribution function for the Pb−Pb pairs is sketched in Figure S24 and indicates that the Pb−Pb bond distances are similar in both domains.

added, past a range of concentrations that enabled the ideal growth of heterostructures (Figure S10b,c), the latter were still formed, but their size and shape distributions worsened considerably; additionally, PbS NCs appeared as a byproduct (Figure S10d). A controlled amount of lead oleate was also critical to prepare well-defined heterostructures. With excessive addition of lead oleate, isolated $Pb_4S_3Br_2$ particles were found as a byproduct (Figure S11).

To understand the growth mechanism, syntheses were run at varying reaction times, while all other reaction conditions were kept constant (including the synthesis temperature, always set at 200 °C). The TEM images of the sample obtained after 30 s of reaction time evidenced nearly cube-shaped NCs containing higher contrast domains (presumably $Pb_4S_3Br_2$) at their edges (Figure S12a). These higher contrast domains further grew in sizes at longer reaction times, while the perovskite domain remained nearly the same (Figure S12a−e). This trend was confirmed by optical absorption spectra of the corresponding samples (dominated by the features from $CsPbBr_3$), which remained almost unchanged over the course of the reaction (Figure S13). By crossing the TEM images and optical absorption data of various samples prepared with different reaction times, we conclude that the perovskite domains formed first, followed by the growth of $Pb_4S_3Br_2$. The optimal reaction time was around 3 min.

The $CsPbBr_3$ clusters that were used as "precursors" for the perovskite domain have a large surface-to-volume ratio; hence, their dissolution during the synthesis of the heterostructures should release a certain amount of oleylammonium ions. This is, however, negligible compared to the amount of oleate that was added (as lead oleate) together with the $CsPbBr_3$ clusters. To test the influence of higher concentrations of oleylammonium ions, we also attempted the synthesis of $CsPbBr_3$−$Pb_4S_3Br_2$ heterostructures under the same conditions as in the synthesis of Figure 1b,c and Figures S2−S5, but with the extra addition of 10^{-2} mmol of OLAM-Br. These attempts failed at producing heterostructures. TEM analysis revealed that the product was mainly represented by $CsPbBr_3$ nanoplatelets/lamellar structures (Figure S14).

As a final test, we also attempted to synthesize $CsPbBr_3$−$Pb_4S_3Br_2$ heterostructures by following conventional hot injection-based syntheses used for the preparation of halide perovskite NC, that is, not employing preformed $CsPbBr_3$ nanoclusters,[5,32,33] but none of them was successful (Figure S15). Therefore, we inferred that a controlled growth of the heterostructures was possible only through the use of $CsPbBr_3$ nanoclusters, most likely as they prevent a massive homogeneous nucleation of perovskite NCs, separately from the chalcohalide NCs.

Characterization by Electron Microscopy. Detailed analyses were performed on single heterostructures through high-resolution, high-angle annular dark field scanning TEM (HAADF-STEM) imaging. Figure 2a represents a high-resolution HAADF-STEM image of a typical $CsPbBr_3$−$Pb_4S_3Br_2$ heterostructure. Both domains were single crystalline. The chalcohalide domain is facing the [101] zone axis, as demonstrated by its Fourier transform (FT, Figure S16), and is attached to one of the facets of the $CsPbBr_3$ cube-shaped NC. The orthorhombic perovskite domain FT can be matched with either the [101] or [010] zone axes, as those are almost

https://dx.doi.org/10.1021/jacs.0c10916
J. Am. Chem. Soc. 2021, 143, 1435−1446

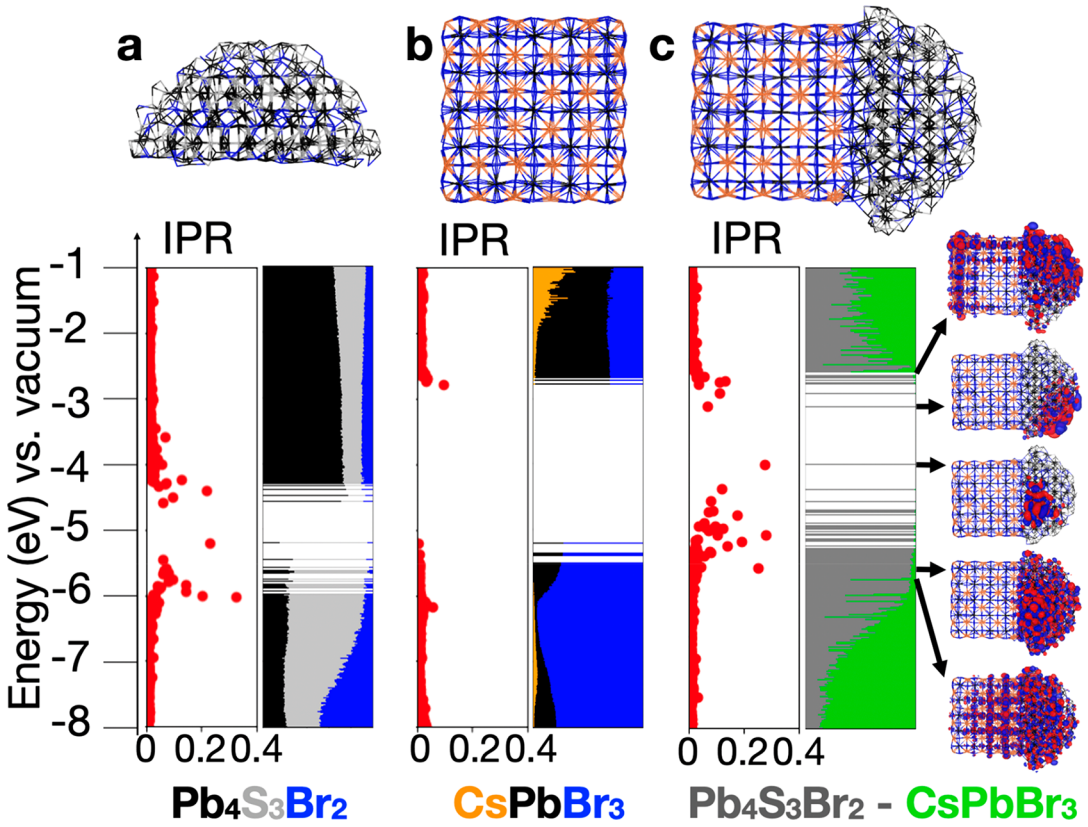

Figure 4. Electronic structure and IPR plots of the (a) $Pb_4S_3Br_2$ half-sphere model, (b) $CsPbBr_3$ cube model, and (c) heterostructure model computed at the DFT/PBE level of theory. The color code indicates the contribution of an atom/moiety type to each molecular orbitals. On the right we plotted both delocalized and localized molecular orbitals at the band edges.

indistinguishable because of the small deviation from the ideal cubic symmetry. The same is true for (101) and (010) planes, which are the planes exposed by the facets of NCs. From a close scrutiny of several heterostructures, we found that the lead chalcohalide domains can grow most commonly on the (101) facets and less commonly on the (010) and (001) facets of the orthorhombic $CsPbBr_3$ perovskite NC, with a mutual orientation of the two domains such that there is little or nearly no mismatch between the joining planes (Figures S17−S19). It is also interesting that although the $CsPbBr_3$ NCs present several sets of equivalent facets, basically all the heterostructures that we could observe were made of only one domain of chalcohalide, and not of multiple domains, attached to a $CsPbBr_3$ NC. This behavior is most likely due to a slow nucleation kinetics of the chalcohalide on the surface of the perovskite NC. Our interpretation is that as soon as a nucleus of chalcohalide is formed on one facet of a $CsPbBr_3$ NC, the energetic barrier for its further accretion is much lower than the energetic barrier for the formation of other chalcohalide nuclei on the other facets.

We then quantitatively analyzed the intensities of the individual atomic columns in a single heterostructure by using STAT-STEM.[34] In an HAADF-STEM image, the intensity of an atomic column depends on the material thickness (amount of atoms composing the column) and its atomic composition (Z number). Panels d and e of Figure 2 show the intensities of the Pb−Br and Cs columns of the perovskite domain, while panels f and g of Figure 2 represent the Pb column intensities of sublattices 1 and 2 from the $Pb_4S_3Br_2$ domain, respectively. The relatively homogeneous distribution confirmed the single-phase character of both the perovskite and the lead chalcohalide domains. Notably, the atomic columns located at the interface presented higher intensities, especially the Cs columns and the columns belonging to the sublattice 2 of the $Pb_4S_3Br_2$ domain (Figure 2e,f). The intensity of the atomic columns located at the boundary of two materials can be affected by local strain that can change the alignment of the atoms, which in turn modifies the channeling effect that is at the base of the HAADF-STEM signal.[35] In this specific case, such rearrangement appears to bring the atoms close to a perfect alignment in the specific zone axis along which the heterostructure is being imaged.

The compositional analysis by energy dispersive X-ray spectroscopy (STEM-EDX) of individual heterostructures attested a uniform distribution of the corresponding elements in the respective domains and returned elemental ratios of Cs:Pb:Br equal to 1.05:1:2.7 for the perovskite domain and of Pb:S:Br equal to 4:2.9:2.6 for the lead chalcobromide domain (Figure S20). These values are in line with the respective stoichiometries of the two materials (i.e., $Pb_4S_3Br_2$ and $CsPbBr_3$). This was further supported by an EDX-line scan across a single heterostructure (Figure S21) which evidenced that the Cs signal was localized in the perovskite domain and the S signal was mainly present in the $Pb_4S_3Br_2$ domain.

A close look at the epitaxial relationship between the two domains, as sketched in Figure 2b, reveals that the lead and bromide ions in the perovskite are aligned with those of the chalcobromide. This is made clearer in Figure 3, showing how the interface monolayer of $Pb_4S_3Br_2$ presents an atomic arrangement similar to the perovskite orthorhombic lattice if

https://dx.doi.org/10.1021/jacs.0c10916
J. Am. Chem. Soc. 2021, 143, 1435−1446

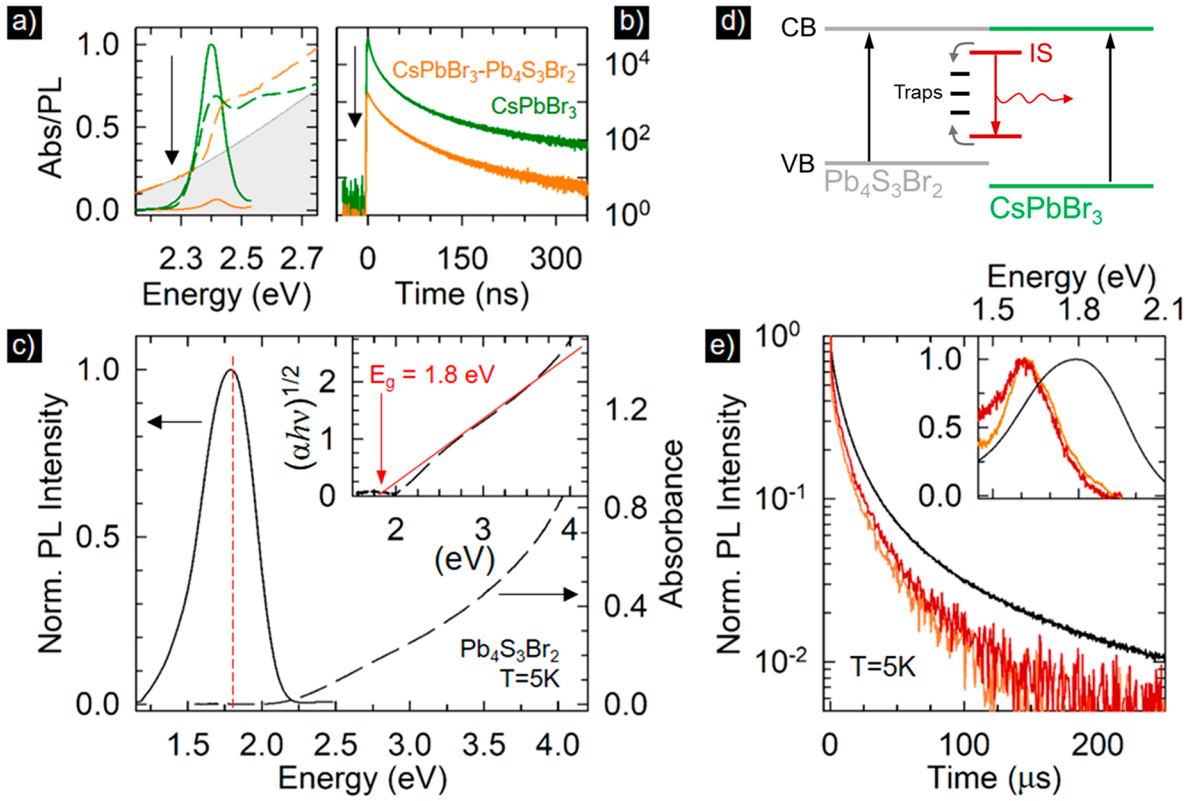

Figure 5. (a) Optical absorption PL spectra and (b) time-resolved PL decay curves of colloidal dispersions of $CsPbBr_3$ NCs and $CsPbBr_3$–$Pb_4S_3Br_2$ heterostructures (normalized to the intensity of bare $CsPbBr_3$ NCs). Green lines refer to $CsPbBr_3$ NCs, and orange lines refer to the heterostructure. The arrow highlights the quenching of the PL intensity in the heterostructure. (c) Optical absorption and PL spectra of $Pb_4S_3Br_2$ NCs (excitation at 3.5 eV). Inset: respective Tauc plot showing the linear dependence (red line) of $(\alpha h\nu)^{1/2}$ with the photon energy typical for indirect band gap transitions. The red arrow indicates the band gap energy that corresponds to the PL peak position. (d) Schematic depiction of the energy levels of the $CsPbBr_3$–$Pb_4S_3Br_2$ heterostructure highlighting the radiative recombination (red arrow) in interface localized states (IS) following excitation of either the perovskite or chalcobromide domains and the respective quenching by traps. (e) Time decay curves of the $Pb_4S_3Br_2$ PL from $CsPbBr_3$–$Pb_4S_3Br_2$ NCs at T = 5 K upon 2.33 and 3.5 eV excitation energy (orange and red lines, respectively) compared to the PL decay curve of bare $Pb_4S_3Br_2$ NCs (black line). Inset: PL spectra of $CsPbBr_3$–$Pb_4S_3Br_2$ NCs at T = 5 K upon 2.33 and 3.5 eV excitation energy (orange and red lines, respectively) compared to the PL spectrum of $Pb_4S_3Br_2$ NCs at the same temperature.

one focuses on the Pb atoms only. Figure S22 contains additional sketches that help to better visualize the epitaxial connection at the interface. The sketches show the connectivity of the cationic substructure at the interface in three different orientations. In the same figure, we also highlight the shared plane of lead atoms that is found almost unaltered within both the chalcohalide and the perovskite structures, pointing to an epitaxial interface. A model of the heterojunction in *.xyz* format is also provided as Supporting Information.

DFT Modeling. The models discussed above give us important hints on how to build a model of the heterostructure for our DFT calculations. For the $CsPbX_3$ perovskite cube we have simply taken one of our "trap-free" models of about 3.2 nm in size published earlier,[29] whereas for the lead chalcohalide we first cleaved the bulk into a sphere of 4.2 nm diameter with a charge balanced stoichiometry (Figure 3a), and then we relaxed the structure and computed its density of states. This shows a large number of surface defects, as evidenced by the inverse participation ratio (IPR) analysis (Figure 4a). IPR with values deviating significantly from zero provide a fingerprint for the presence of localized states in the electronic structure, which in the case of chalcohalide are mostly present at the conduction band (CB) and valence band (VB) edges. For comparison, the IPR analysis for the perovskite systems exhibits only delocalized states, as expected (Figure 4b). IPR values can also be used to filter trap states in the electronic structure and deduce the actual intake of the CB and VB edges, here extrapolated (with IPR below 0.03) at about 1.6–1.7 eV (Figure 4a), in good agreement with the experimental value for the emission of 1.6–1.8 eV for $Pb_4S_3Br_2$ (see the discussion on the optical properties).

Note that as in the case of lead halide perovskites our DFT approach provides the correct band gap for the wrong reason: the lack of spin–orbit coupling in our calculations, which lowers the band gap but is computationally prohibitive for the heterostructure size, is compensated by the typical band gap underestimation for pure exchange-correlation functionals like the Perdew–Burke–Ernzerhof (PBE) employed here. The choice of IPR below 0.03 is arbitrary; however, it does indicate that trap states are present in various kinds, from very localized to less localized ones. After we assessed this part, we cut half of the chalcohalide sphere, relaxed it, and arranged it on top of the perovskite domain, following the alignment proposed above and sketched in Figure 3b,c. The relaxation of the heterostructure occurred smoothly, an indication that the structural alignment between the two domains was indeed the correct one.

We then computed the electronic structure and the density of states followed by the IPR analysis. As expected, by looking

https://dx.doi.org/10.1021/jacs.0c10916
J. Am. Chem. Soc. 2021, 143, 1435–1446

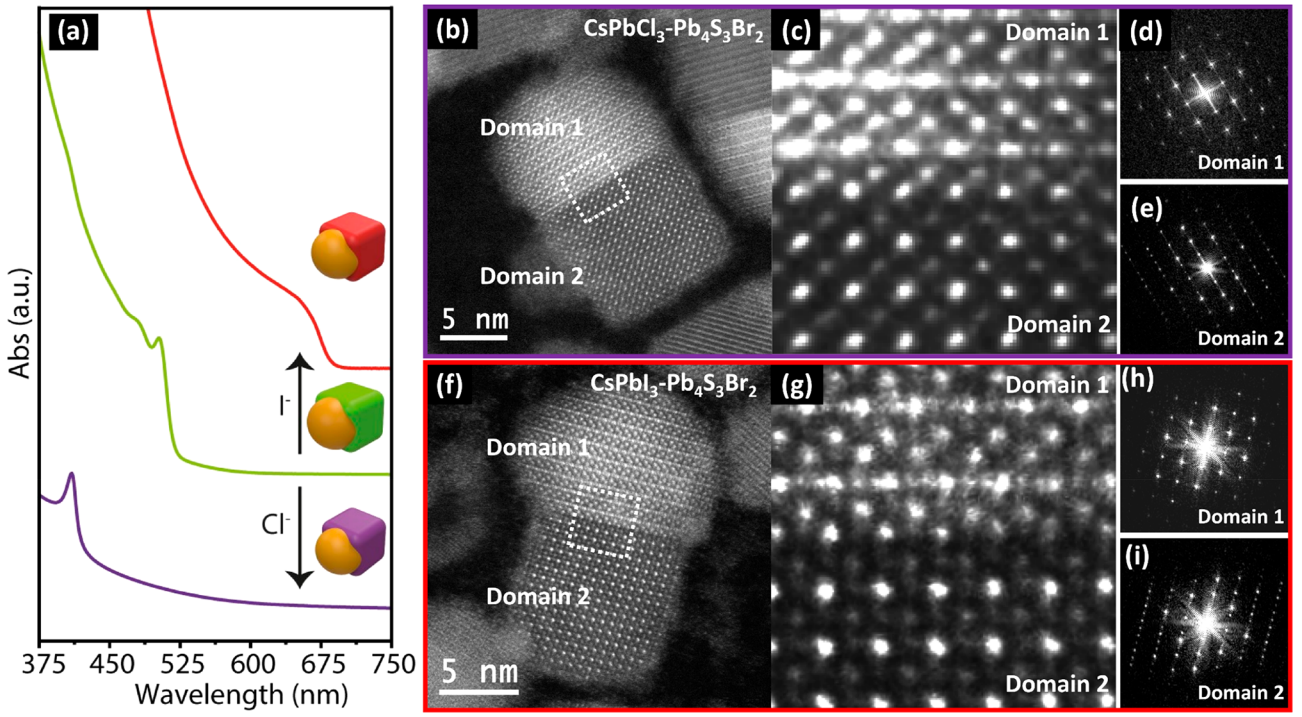

Figure 6. (a) Optical absorption spectra of pristine $CsPbBr_3$−$Pb_4S_3Br_2$ NCs and of the same NCs after halide exchange with either Cl− or I− recorded in colloidal dispersions. (b) HRSTEM image of $CsPbCl_3$−$Pb_4S_3Br_2$ NC. (c) Magnified image of the region highlighted in white dotted line. (d) and (e) show the FT of the regions labeled as domain 1 and domain 2 in (b), respectively. (f) HRSTEM image of a $CsPbI_3$−$Pb_4S_3Br_2$ NC. (g) Magnified image of the region highlighted in white dotted lines. (h) and (i) show the FTs of the domains labeled as domain 1 and domain 2 of panels f and g. The $CsPbCl_3$ and $CsPbI_3$ domains were in the [100] and [101] orientation, while the $Pb_4S_3Br_2$ domain was in the [101] orientation, respectively, with respect to the viewing direction.

at the electronic structure of the domains computed separately, the CB edge of the heterostructure is apparently dominated by the $Pb_4S_3Br_2$ domain. Notably, although the band edge is fully defined by trap states, as expressed by the IPR values, the first delocalized states in the CB are present in both the chalcohalide and perovskite domains. To make this clear, we plotted the molecular orbitals for both the localized states and the first of the delocalized one (Figure 4c). Conversely, in the valence band region, the orbital contribution is different. The first states at the VB edge are still mostly localized in the chalcohalide domain, pointing toward the presence of an energy offset with the perovskite domain. The first delocalized molecular orbitals deeper in the VB appear intermixed, with some present only on the chalcohalide domain and others delocalized on both domains (Figure 4c). States even deeper exhibit mostly mixing between the two domains. Notably, there are no states at the VB edge region that belong solely to the perovskite domain. Overall, following the core−shell nomenclature,[36] these data suggest that the energy level alignment of the heterostructure is quasi-type II, with the VB localized on the chalcohalide domain and the CB mixed between the two domains.

Optical Properties. On the basis of theoretical insights provided by DFT, we proceeded to investigate the excitonic processes of the $CsPbBr_3$−$Pb_4S_3Br_2$ heterostructures. To this end, we prepared pure $CsPbBr_3$ and $Pb_4S_3Br_2$ NCs of nearly the same size as the respective domains in the heterostructure (namely, $CsPbBr_3$NCs having an edge length of 14 nm and $Pb_4S_3Br_2$ NCs with a diameter of 8.5 nm) and performed side-by-side optical spectroscopy experiments. The optical spectra for $CsPbBr_3$ NCs and related heterostructures are shown in Figure 5a. As anticipated, the pure $CsPbBr_3$ NCs featured the typical sharp absorption edge and a nearly resonant PL peak with PLQY = 67 ± 7%. The PL dynamic followed a multiexponential decay with effective lifetime of ∼10 ns (Figure 5b). The spectral properties of the $Pb_4S_3Br_2$ NCs are reported in Figure 5c and show a nearly featureless absorption spectrum typical of an indirect band gap material,[29] as confirmed by the Tauc plot in the inset of Figure 5c, showing a linear dependence of the absorption profile on the square root of $(\alpha h\nu)$, where α is the absorption coefficient and $h\nu$ the energy of the incident photons. The fitting yields a band gap energy of ∼1.8 eV, in good agreement with the band gap energy estimated by DFT (Figure 4a). The broad PL spectrum was also peaked at ∼1.8 eV, thus indicating that the radiative recombination is due to an indirect transition coupling the band edge states, possibly promoted by partial relaxation of momentum conservation in nanoscale systems. The PLQY at room temperature was <1%, likely due to nonradiative quenching by carrier trapping in surface defects. Cooling the $Pb_4S_3Br_2$ NCs to cryogenic temperatures strongly suppressed such nonradiative losses, resulting in a substantial enhancement of the PL intensity at T = 5 K, accompanied by a concomitant lengthening of the PL lifetime that increased from 70 ns to 4.1 μs (Figure S25). This behavior suggests a recombination from an indirect transition.

Combining the $Pb_4S_3Br_2$ and $CsPbBr_3$ domains in the heterostructure strongly quenches the emission from both domains. The quenching of the PL from $CsPbBr_3$ in the heterostructure is consistent with an ultrafast hole transfer from the perovskite domain to the $Pb_4S_3Br_2$ domain (Figure 5d). The very weak green PL that was observed from the

https://dx.doi.org/10.1021/jacs.0c10916
J. Am. Chem. Soc. 2021, 143, 1435−1446

sample of heterostructures had the same spectral position and decay kinetics as the sample of pure $CsPbBr_3$ NCs (Figure 5a,b). Hence, we ascribe this residual PL to the presence of isolated $CsPbBr_3$ NCs in the sample of heterostructures. Interestingly, by cooling the heterostructures to $T < 70$ K, an emission peak at 1.60 eV emerged, either under direct excitation of the $CsPbBr_3$ domain at 2.33 eV (that is, below the band gap of the $CsPbBr_3$ NCs) or under UV excitation at 3.5 eV. This emission was red-shifted by ∼200 meV from that observed, at the same temperature, in the sample of pure $Pb_4S_3Br_2$ NCs and was thus ascribed to the recombination from intragap localized states in the heterostructures, consistent with the DFT analysis in Figure 4c. No such emission was observed from the heterostructures at room temperature, indicating substantial nonradiative losses, likely associated with carrier trapping. Also, the PL decay at 5 K associated with such 1.6 eV emission from the heterostructures was faster than the PL decay of the 1.8 eV emission from the $Pb_4S_3Br_2$ NCs (1.6 μs vs 4.1 μs) and was identical under either excitation conditions (2.33 and 3.5 eV). This behavior suggests that in the heterostructure the PL dynamics does not depend on the regions of the heterostructure where the photocarriers are initially generated and confirms the quenching effect of the interface.

$CsPbCl_3$–$Pb_4S_3Br_2$ and $CsPbI_3$–$Pb_4S_3Br_2$ Heterostructures. The exposure of the $CsPbBr_3$–$Pb_4S_3Br_2$ heterostructures to either Cl^- or I^- ions resulted in anion exchange, as evidenced by the changes in the optical absorption spectra (Figure 6a). Notably, the Cl-treated sample exhibited a more evident absorption feature toward longer wavelengths in addition to the band edge absorption of the $CsPbCl_3$ domain. This tail, arising from the chalcohalide domain, is partially hidden in the initial sample and completely hidden in the iodide-exchanged sample. Morphological analysis by TEM showed that the NCs retained nearly the same size and shape as the initial NCs after anion exchange (Figure S26). Compositional mapping of individual heterostructures by STEM-EDX to assess anion distribution evidenced a clear segregation of the Cl and the Br signals in the two domains of the heterostructures (Figure S27), with Cl preferentially segregated in the perovskite domain and Br in the chalcohalide domain, compatible with a $CsPbCl_3$–$Pb_4S_3Br_2$ composition for the heterostructure. Similar conclusions were drawn from EDX line scans on the heterostructures reacted with I^- ions (Figure S28), suggesting a $CsPbI_3$–$Pb_4S_3Br_2$ composition in the latter case. HAADF-STEM analyses of these two samples revealed again a sharp interface between the two domains (Figure 6b–i), with the same epitaxial relationships as in the $CsPbBr_3$–$Pb_4S_3Br_2$ sample discussed earlier (Figure 2), evidencing that anion exchange had not disrupted the overall structure of the initial $CsPbBr_3$–$Pb_4S_3Br_2$ NCs. The sharpness of the interface was also obvious from the intensity maps of the various columns in the perovskite and chalcohalide domains in representative heterostructures belonging to these two samples (Figure S29). This was confirmed by the FT of the cubic $CsPbCl_3$ domain displayed in Figure 6d along its [100] zone axis and is in agreement with the XRPD analysis of the same sample (Figure S30). The FT of the iodide exchange sample is reported in Figure 6h and does not show the additional diffraction spots typical of an orthorhombic structure whereas the chalcohalide domains was found to be unaffected, retaining the $Pb_4S_3Br_2$ phase. The XRPD pattern of the iodide-exchanged sample unambiguously conformed to the "black" orthorhombic perovskite phase of $CsPbI_3$ (Figure S30).[37]

As a further control, the attempt at halide exchange on pure $Pb_4S_3Br_2$ NCs left the NCs unaltered (see Figure S31 comparing optical absorption, XRPD, and TEM data of $Pb_4S_3Br_2$ NCs before and after treatment with either Cl^- or I^- ions). Taken together, these sets of data indicate that anion exchange took place only in the halide perovskite region of the heterostructures. The electronic structure and IPR analysis of these systems shows that also for the lead chloride and iodide perovskites the energy alignment is quasi-type II, with features similar to those of the bromide case (Figure S32).

Extensive spectroscopic analysis was performed on these two heterostructures as well, revealing, in both cases nearly complete quenching of the PL from the perovskite domain, as observed for the $CsPbBr_3$–$Pb_4S_3Br_2$ systems. Notably, no acceleration was observed also for the kinetics of the $CsPbCl_3$ domain in the heterostructures with respect to the isolated $CsPbCl_3$ NCs. These kinetics, because of their fast decay time, were measured by using a streak camera with temporal resolution better than 7 ps (Figure S33), thus confirming the ultrafast nature of the hole transfer process.

One interesting question that arises in these nanostructures is whether the presence of the chalcohalide domain has any influence on the structural stability of the perovskite domain. This is particularly insightful for the "black" γ-$CsPbI_3$ phase, as this structure is metastable at room temperature and quickly undergoes a transition to the nonemitting "yellow" δ-$CsPbI_3$ phase in the case of colloidal NCs (on a time span of hours/days). The "yellow" δ-$CsPbI_3$ phase is characterized by linear arrays of edge-sharing $[PbI_6]^{4-}$ octahedra, very much different structurally from the perovskite structure. By monitoring the stability of the $CsPbI_3$–$Pb_4Br_3S_2$ NCs both as colloidal dispersions and as solids films over time under air, and through a comparison with $CsPbI_3$ NCs of nearly the same size, we found the following: the $CsPbI_3$ NCs, as already well established, were very unstable, since they transformed to the yellow phase already within 1 day of storage under air, as revealed by XRPD analysis (Figure S34). On the other hand, after several days of aging, colloidal suspensions of $CsPbI_3$–$Pb_4Br_3S_2$ heterostructures did not show any relevant change, neither in their optical features and morphology (Figure S35) nor in their XRPD patterns (Figure S36). Importantly, in the XRPD patterns of Figure S36 there are no additional diffraction peaks observed that belong to the δ-$CsPbI_3$ phase, even after 3 weeks of aging under air. We ascribe this structural stability to the presence of the interface joining $CsPbI_3$ and $Pb_4S_3Br_2$. This interface most likely confers higher structural rigidity to the perovskite $CsPbI_3$ lattice, preventing the reorganization both of the substructure of $[PbI_6]^{4-}$ octahedra and of the Cs^+ ions that would be necessary for the transition to the δ-$CsPbI_3$ phase to take place. This reorganization would disrupt the epitaxial connection of the two lattices, creating a new interface characterized by a much higher interfacial energy. Indeed, a hypothetical interface between the "yellow-phase" δ-$CsPbI_3$ and $Pb_4S_3Br_2$ heterostructure is extremely unlikely to exist: our observations demonstrate that the interfaces that we observe experimentally are based on the sharing of a plane of lead ions which produces a square pattern, as shown in Figure 3c and Figure S37. Such a squared plane of lead is not found in δ-$CsPbI_3$ in any orientation. Our conclusion is that the transformation of black $CsPbI_3$ into its

https://dx.doi.org/10.1021/jacs.0c10916
J. Am. Chem. Soc. 2021, 143, 1435–1446

yellow polymorph is impossible without disrupting the heterostructure.

CONCLUSIONS

In conclusion, we have reported the synthesis of a series of $CsPbX_3$–$Pb_4Br_3S_2$ heterostructures and have studied their growth mechanisms as well as their structural and optical features and modeled their overall electronic structure. One likely reason for the affinity of this specific chalcohalide with lead halide perovskites is that its sublattice of Pb cations is similar to that of the perovskite, so that epitaxial heterostructures can be grown. In the present synthesis scheme, the use of preformed, subnanometer $CsPbBr_3$ clusters appears to be a very valuable strategy for preparing the initial $CsPbBr_3$–$Pb_4Br_3S_2$ heterostructures, from which the other two have been derived by selective anion exchange in the perovskite domain. It is likely that this synthesis strategy can be extended to other nanocrystal heterostructures containing a halide perovskite domain, providing new ground for materials scientists to develop new types of nanoscale materials. On the other hand, it remains to be seen whether other chalcohalides, not based on Pb, can also form heterostructures with lead halide perovskites as easily as in the present case. One potential issue is that the introduction of another cation, instead of Pb^{2+}, in the reaction environment, might render the lead halide perovskite unstable. There is also ample space for improving the optical properties of the nanocrystals developed in this present work, and a finer control of the interfacial structure could unlock the full potential of these heterostructures for optoelectronic or photonic applications. Finally, the increased structural rigidity conferred to the perovskite lattice by virtue of an epitaxial interface with another material is a fascinating aspect of these nanostructures and can provide a possible avenue for mitigating the well-known instability of halide perovskites.

EXPERIMENTAL SECTION

Chemicals. 1-Octadecene (ODE, tech, 90%), oleic acid (OA, tech, 90%), oleylamine (OLA, tech, 70%), lead(II) bromide ($PbBr_2$, 98%), lead(II) chloride ($PbCl_2$, 98%), lead(II) iodide (PbI_2, 98%), cesium carbonate (Cs_2CO_3, 99%), dodecanethiol (DDT, 99.9%), sulfur powder (S, 99.99%), and lead acetate trihydrate ($Pb(OAc)_2{\cdot}3H_2O$, 99.99%), were purchased from Sigma-Aldrich. All reagents were used as received without any further experimental purification.

Preparation of Cs-Oleate Precursor. In a typical synthesis, Cs_2CO_3 (0.652 g, 2 mmol), OA (2.5 mL, 7.5 mmol), and ODE (17.5 mL) were loaded into a 50 mL three-neck flask, dried for 1 h at 110 °C, and then heated under N_2 to 150 °C until the solution turned clear. The resulting mixture was transferred into a N_2-filled glass vial and was stored inside a glovebox for further use.

Preparation of $PbBr_2$ Stock Solution. $PbBr_2$ powder (0.734 g, 2 mmol), OA (5 mL), and OLA (5 mL) were mixed with ODE (30 mL) in a 100 mL three-neck round-bottom flask. The reaction mixture was dried/degassed under vacuum for 30 min at 110 °C. Then, the flask was filled with N_2, and the temperature was raised to 150 °C. After complete dissolution of $PbBr_2$ salt, the solution was cooled to room temperature (25 °C) and transferred into a N_2-filled glass vial.

Preparation of $Pb(OA)_2$ Stock Solution. $Pb(OAc)_2{\cdot}3H_2O$ powder (0.76 g, 2 mmol) and OA (1.3 mL) were mixed with ODE (18.7 mL) in a 50 mL three-neck round-bottom flask. The reaction mixture was degassed under vacuum for 1 h at 110 °C and then heated under N_2 to 150 °C until all $Pb(OAc)_2{\cdot}3H_2O$ reacted with OA. Thereafter, the solution was cooled to room temperature (25 °C) and transferred into N_2-filled glass vials.

Preparation of S-ODE Stock Solution. 1.5 mmol of S powder was mixed with 15 mL ODE (predegassed at 120 °C for an hour) in a 20 mL glass vial inside a glovebox. Then, the resulting mixture was sonicated until the complete dissolution of S.

Synthesis of $CsPbBr_3$ Nanoclusters. $CsPbBr_3$ nanoclusters were synthesized following a previously reported method.[30] Briefly, 4 mL of the above-mentioned $PbBr_2$ stock solution was transferred into the N_2-filled 20 mL glass vial. Thereafter, 0.2 mL of Cs-oleate stock solution was injected into the $PbBr_2$ stock solution, and the resulting mixture was kept under stirring at room temperature (25 °C). After about 30 min, the resulting mixture was centrifuged at 8000 rpm for 5 min, the supernatant was discarded, and the precipitate was redispersed in 0.9 mL of degassed ODE.

Synthesis of $CsPbBr_3$–$Pb_4S_3Br_2$ Heterostructures. In a typical synthesis, 4.0 mL of degassed ODE was added to a 20 mL glass vial under the N_2. Then the vial was heated to 200 °C, and 100 μL of the above-mentioned $Pb(OA)_2$ solution and 20 μL of DDT were added into the reaction system. Then, the mixture of S (0.1 mL) and $CsPbBr_3$ nanoclusters (0.9 mL) was swiftly injected into the reaction mixture. The reaction was allowed to proceed for 3 min and was subsequently quenched by immersing the vial in an ice water bath. Thereafter, the NCs were collected by centrifugation at 6000 rpm for 5 min, the supernatant was discarded, and the precipitate was redispersed in 5 mL of anhydrous toluene. The toluene dispersion of the NCs was centrifuged once again (at 4000 rpm for 5 min), the colloidally unstable fraction was discarded, and the supernatant was collected for further use.

Synthesis of $Pb_4S_3Br_2$ Nanocrystals. In a typical synthesis, 4.0 mL of degassed ODE was added to a 20 mL glass vial under the N_2. Then the vial was heated to 150 °C, and 400 μL of the above-mentioned $PbBr_2$ solution and 100 μL of DDT were separately added into the reaction system. Then 100 μL of the above-mentioned S-ODE solution was swiftly injected, and the reaction mixture was annealed for 5 min at 150 °C. Subsequently, the mixture was cooled to room temperature and centrifuged at 4000 rpm for 5 min. After centrifugation, the precipitate was discarded, and the supernatant was centrifuged again (8000 rpm for 5 min) by adding 10 mL of acetone. Thereafter, the precipitate was redispersed in toluene for further use.

Synthesis of $CsPbBr_3$ Nanocrystals. In a typical synthesis, 4.0 mL of ODE was added to a 20 mL glass vial under the air and heated to 150 °C; then 1.0 mL of the above-mentioned seed cluster solution ($CsPbBr_3$, without S-ODE) was swiftly injected, and the mixture was annealed for 3 min and cooled subsequently by using an ice water bath. Then, the resulting mixture was centrifuged at 8000 rpm for 5 min, the supernatant was discarded, and the precipitate was dispersed in 4 mL of toluene.

Anion Exchange Reactions. All the anion exchange reactions were performed under ambient conditions following previously reported methods.[38,39] Briefly, 2 mL of the $CsPbBr_3$–$Pb_4S_3Br_2$ heterostructures ($CsPbBr_3$ or $Pb_4S_3Br_2$ NCs) solution was added into a 10 mL glass vial, and different amounts of PbX_2 stock solution (ranging from 30 to 300 μL) were added under vigorous stirring at RT to obtain the desired emission color. Thereafter, the heterostructures were collected by centrifugation at 6000 rpm for 5 min and redispersed in toluene for further use.

X-ray Powder Diffraction (XRPD) Characterization. The XRPD analysis was performed on a PANanalytical Empyrean X-ray diffractometer, equipped with a 1.8 kW Cu Kα ceramic X-ray tube, operating at 45 kV and 40 mA, and a PIXcel^{3D} 2 × 2 area detector. To avoid preferred orientation effect, the concentrated dispersions of NCs were mixed with fumed silica powder prior to their deposition on zero-diffraction silicon substrate. All the diffraction patterns reported in this work were collected at room temperature under ambient conditions by using parallel beam geometry and symmetric reflection mode. Postacquisition XRPD data analysis was performed by using the HighScore 4.1 software from PANalytical.

Transmission Electron Microscopy (TEM) Characterization. Bright-field TEM images of the NC samples were acquired with a JEOL-1100 transmission electron microscope operating at an acceleration voltage of 100 kV. Samples were prepared by drop-

https://dx.doi.org/10.1021/jacs.0c10916
J. Am. Chem. Soc. 2021, 143, 1435–1446

casting diluted solutions of NCs onto carbon film-coated 200 mesh copper grids for low-resolution TEM.

High-Resolution TEM and Energy Dispersive X-ray Spectroscopy. The characterization was performed by using a JEOL JEM2200 image corrected instrument operated at 200 kV and equipped with an in-column Omega energy filter and Bruker Quantax 400 EDX system with a 60 mm^2 XFlash detector. Partial HRSTEM and EDS characterization was taken on a ThermoFisher Scientific Titan Cubed Themis G2 300 transmission electron microscope with an acceleration voltage of 300 kV and equipped with a Super-X4 probe super energy spectrum.

High-Resolution High Angle Annular Dark Field Scanning Transmission Electron Microscopy Characterization. High-resolution HAADF-STEM images were acquired with a probe-corrected cubed Thermo Fisher Scientific Titan microscope operating at 300 kV with a probe semiconvergence angle of 20.5 mrad. Qualitative analyses of column intensities were performed by using STAT-STEM.[34] The total scattered intensity and location of all atomic columns were determined by fitting Gaussian functions to these columns.

Computational Modeling. For the electronic structure calculations, we have performed atomistic simulations at the density functional theory (DFT) level using the PBE exchange−correlation functional[40] and a double-ζ basis set plus polarization functions on all atoms as implemented in the CP2K 6.1 package.[41] Scalar relativistic effects were incorporated as effective core potential functions in the basis set. All structures have been optimized in a vacuum. More details on how the models were built can be found in the main text. To identify surface localized states that could trap charge carriers, we have also computed the inverse participation ratio (IPR)[42] for the chalcohalide and perovskite systems alone and in the heterostructure. The IPR, as also demonstrated for other nanocrystals,[43] quantifies the orbital localization of a given molecular orbital and is defined as

$$\mathrm{IPR}_i = \frac{\sum_\alpha |P_{\alpha,i}|^4}{\left(\sum_\alpha |P_{\alpha,i}|^2\right)^2}$$

Here, $P_{\alpha,i}$ represents the weight of molecular orbital i on a given atom α expanded in an atomic orbital basis. For finite systems, the IPR provides an estimate of the number of atoms that contribute to a given electronic state i. It can range from the inverse of the number of atoms in the system when the wave function is distributed equally over all atoms in the system to 1 in the case of a localized state to a single atom. When values are near zero, the IPR identifies delocalized states.

Spectroscopic Studies. Optical absorption spectra were recorded on a Varian Cary 50 Scan UV−vis spectrophotometer under normal incidence in quartz cuvettes (optical path 0.1 cm). Absolute photoluminescence quantum yields of NC samples were measured by using an Edinburgh FLS900 fluorescence spectrometer equipped with a xenon lamp and a monochromator. The PLQY was measured by using a calibrated integrating sphere (λ_{ex} = 350 nm for all $CsPbX_3$ and $CsPbX_3$-$Pb_4S_3Br_2$ (X = Cl, Br) samples while the λ_{ex} = 450 nm was used for $CsPbI_3$ /$CsPbI_3$−$Pb_4S_3Br_2$ NCs). All NC dispersions were diluted to an optical density of 0.1 at the corresponding excitation wavelength to minimize the amount of fluorophore being reabsorbed. The PL and PL dynamics were investigated by using a TM-C10083CA Hamamatsu spectrometer and a Hamamatsu R943-02 time-correlated single-photon counting unit coupled to an Oriel Instruments Cornerstone 260 monochromator using either an Edinburgh Inst. EPL 405 pulsed diode laser (λ_{exc} = 405 nm, pulse duration 40 ps, variable repetition rate) or a frequency-tripled/doubled pulsed Nd:YAG laser (λ_{exc} = 355/532 nm, pulse duration 5 ns, repetition rate 140 Hz) as excitation sources. The PL and time-resolved PL experiments on $CsPbCl_3$ and $Pb_4S_3Br_2$−$CsPbCl_3$ NCs were performed by using a frequency-doubled Ti:sapphire laser (λ_{exc} = 360 nm, pulse duration 150 fs, and repetition rate 76 MHz) as excitation source and a Hamamatsu streak camera as detector. To perform optical experiments at cryogenic temperatures, the NCs were drop-casted onto glass substrates and placed in a variable-temperature insert of a closed-cycle helium cryostat (T = 3.5−300 K).

■ ASSOCIATED CONTENT

Supporting Information

The Supporting Information is available free of charge at https://pubs.acs.org/doi/10.1021/jacs.0c10916.

Detailed results of various control experiments including reaction temperature, role of various ligands and precursors on the formation of heterostructure, optical absorption, PL, PLQY, and PL decay curves, XRPD patterns, EDS compositional analysis, HR-TEM/STEM images, and computational analysis (PDF)

3D model of the heterojunction (XYZ)

■ AUTHOR INFORMATION

Corresponding Authors

Jun Song − *Center for Biomedical Optics and Photonics (CBOP) & College of Physics and Optoelectronic Engineering, Key Laboratory of Optoelectronic Devices and Systems, Shenzhen University, Shenzhen 518060, P. R. China*; orcid.org/0000-0002-2321-7064; Email: songjun@szu.edu.cn

Ivan Infante − *Department of Nanochemistry, Istituto Italiano di Tecnologia, 16163 Genova, Italy; Department of Theoretical Chemistry, Faculty of Science, Vrije Universiteit Amsterdam, 1081 HV Amsterdam, The Netherlands*; orcid.org/0000-0003-3467-9376; Email: ivan.infante@iit.it

Sara Bals − *Electron Microscopy for Materials Science (EMAT) and NANOlab Center of Excellence, University of Antwerp, 2020 Antwerp, Belgium*; Email: sara.bals@uantwerpen.be

Sergio Brovelli − *Dipartimento di Scienza dei Materiali, Università degli Studi di Milano-Bicocca, 20125 Milano, Italy*; orcid.org/0000-0002-5993-855X; Email: sergio.brovelli@unimib.it

Liberato Manna − *Department of Nanochemistry, Istituto Italiano di Tecnologia, 16163 Genova, Italy*; orcid.org/0000-0003-4386-7985; Email: liberato.manna@iit.it

Authors

Muhammad Imran − *Department of Nanochemistry, Istituto Italiano di Tecnologia, 16163 Genova, Italy*; orcid.org/0000-0001-7091-6514

Lucheng Peng − *Department of Nanochemistry, Istituto Italiano di Tecnologia, 16163 Genova, Italy; Center for Biomedical Optics and Photonics (CBOP) & College of Physics and Optoelectronic Engineering, Key Laboratory of Optoelectronic Devices and Systems, Shenzhen University, Shenzhen 518060, P. R. China*

Andrea Pianetti − *Dipartimento di Scienza dei Materiali, Università degli Studi di Milano-Bicocca, 20125 Milano, Italy*

Valerio Pinchetti − *Dipartimento di Scienza dei Materiali, Università degli Studi di Milano-Bicocca, 20125 Milano, Italy*; orcid.org/0000-0003-3792-3661

Julien Ramade − *Electron Microscopy for Materials Science (EMAT), University of Antwerp, 2020 Antwerp, Belgium*

Juliette Zito − *Department of Nanochemistry, Istituto Italiano di Tecnologia, 16163 Genova, Italy; Dipartimento di Chimica e Chimica Industriale, Università degli Studi di Genova, 16146 Genova, Italy*

https://dx.doi.org/10.1021/jacs.0c10916
J. Am. Chem. Soc. 2021, 143, 1435−1446

Francesco Di Stasio − *Photonic Nanomaterials group, Istituto Italiano di Tecnologia, 16163 Genova, Italy;* orcid.org/0000-0002-2079-3322

Joka Buha − *Department of Nanochemistry, Istituto Italiano di Tecnologia, 16163 Genova, Italy*

Stefano Toso − *Department of Nanochemistry, Istituto Italiano di Tecnologia, 16163 Genova, Italy; International Doctoral Program in Science, Università Cattolica del Sacro Cuore, 25121 Brescia, Italy*

Complete contact information is available at: https://pubs.acs.org/10.1021/jacs.0c10916

Author Contributions

[▽]M.I. and L.P. contributed equally to this work.

Notes

The authors declare no competing financial interest.

■ ACKNOWLEDGMENTS

This work was performed on the Dutch national e-infrastructure with the support of SURF Cooperative. L.P. and J.S. are thankful for the support by the National Key R&D Program of China (2018YFC0910600) and the National Natural Science Foundation of China (61775145). F.D.S. and S.B. acknowledge support by the European Research Council via the ERC-StG "NANOLED" (851794) and the ERC-Cog "REALNANO" (815128). The authors acknowledge financial support from the European Commission under the Horizon 2020 Programme through Grant Agreement No. 731019 (EUSMI). S.B., A.P., and V.P. gratefully acknowledge the financial support from the Italian Ministry of University and Research (MIUR) through grant "Dipartimenti di Eccellenza-2017 Materials For Energy".

■ REFERENCES

(1) Kovalenko, M. V.; Protesescu, L.; Bodnarchuk, M. I. Properties and potential optoelectronic applications of lead halide perovskite nanocrystals. *Science* **2017**, *358* (6364), 745−750.

(2) Sutherland, B. R.; Sargent, E. H. Perovskite photonic sources. *Nat. Photonics* **2016**, *10* (5), 295−302.

(3) Akkerman, Q. A.; Rainò, G.; Kovalenko, M. V.; Manna, L. Genesis, challenges and opportunities for colloidal lead halide perovskite nanocrystals. *Nat. Mater.* **2018**, *17* (5), 394−405.

(4) Quan, L. N.; Rand, B. P.; Friend, R. H.; Mhaisalkar, S. G.; Lee, T.-W.; Sargent, E. H. Perovskites for Next-Generation Optical Sources. *Chem. Rev.* **2019**, *119* (12), 7444−7477.

(5) Protesescu, L.; Yakunin, S.; Bodnarchuk, M. I.; Krieg, F.; Caputo, R.; Hendon, C. H.; Yang, R. X.; Walsh, A.; Kovalenko, M. V. Nanocrystals of Cesium Lead Halide Perovskites ($CsPbX_3$, X = Cl, Br, and I): Novel Optoelectronic Materials Showing Bright Emission with Wide Color Gamut. *Nano Lett.* **2015**, *15* (6), 3692−3696.

(6) Ten Brinck, S.; Zaccaria, F.; Infante, I. Defects in lead halide perovskite nanocrystals: Analogies and (many) differences with the bulk. *ACS Energy Lett.* **2019**, *4* (11), 2739−2747.

(7) Shamsi, J.; Urban, A. S.; Imran, M.; De Trizio, L.; Manna, L. Metal halide perovskite nanocrystals: synthesis, post-synthesis modifications, and their optical properties. *Chem. Rev.* **2019**, *119* (5), 3296−3348.

(8) Gandini, M.; Villa, I.; Beretta, M.; Gotti, C.; Imran, M.; Carulli, F.; Fantuzzi, E.; Sassi, M.; Zaffalon, M.; Brofferio, C.; et al. Efficient, fast and reabsorption-free perovskite nanocrystal-based sensitized plastic scintillators. *Nat. Nanotechnol.* **2020**, *15*, 462−468.

(9) Ijaz, P.; Imran, M.; Soares, M. M.; Tolentino, H. C.; Martín-García, B.; Giannini, C.; Moreels, I.; Manna, L.; Krahne, R. Composition-, size-, and surface functionalization-dependent optical properties of lead bromide perovskite nanocrystals. *J. Phys. Chem. Lett.* **2020**, *11* (6), 2079−2085.

(10) Yuan, J.; Hazarika, A.; Zhao, Q.; Ling, X.; Moot, T.; Ma, W.; Luther, J. M. Metal Halide Perovskites in Quantum Dot Solar Cells: Progress and Prospects. *Joule* **2020**, *4* (6), 1160−1185.

(11) Imran, M.; Ijaz, P.; Baranov, D.; Goldoni, L.; Petralanda, U.; Akkerman, Q.; Abdelhady, A. L.; Prato, M.; Bianchini, P.; Infante, I.; Manna, L. Shape-pure, nearly monodispersed $CsPbBr_3$ nanocubes prepared using secondary aliphatic amines. *Nano Lett.* **2018**, *18* (12), 7822−7831.

(12) Bera, S.; Pradhan, N. Perovskite Nanocrystal Heterostructures: Synthesis, Optical Properties, and Applications. *ACS Energy Lett.* **2020**, *5* (9), 2858−2872.

(13) Kamat, P. V.; Pradhan, N.; Schanze, K.; Weiss, P. S.; Buriak, J.; Stang, P.; Odom, T. W.; Hartland, G. Challenges and Opportunities in Designing Perovskite Nanocrystal Heterostructures. *ACS Energy Lett.* **2020**, *5* (7), 2253−2255.

(14) Balakrishnan, S. K.; Kamat, P. V. Au-$CsPbBr_3$ Hybrid Architecture: Anchoring Gold Nanoparticles on Cubic Perovskite Nanocrystals. *ACS Energy Lett.* **2017**, *2* (1), 88−93.

(15) Zhang, X.; Wu, X.; Liu, X.; Chen, G.; Wang, Y.; Bao, J.; Xu, X.; Liu, X.; Zhang, Q.; Yu, K.; Wei, W.; Liu, J.; Xu, J.; Jiang, H.; Wang, P.; Wang, X. Heterostructural $CsPbX_3$-PbS (X = Cl, Br, I) Quantum Dots with Tunable Vis-NIR Dual Emission. *J. Am. Chem. Soc.* **2020**, *142* (9), 4464−4471.

(16) Chen, W.; Hao, J.; Hu, W.; Zang, Z.; Tang, X.; Fang, L.; Niu, T.; Zhou, M. Enhanced stability and tunable photoluminescence in perovskite $CsPbX_3$/ZnS quantum dot heterostructure. *Small* **2017**, *13* (21), 1604085.

(17) Ravi, V. K.; Saikia, S.; Yadav, S.; Nawale, V. V.; Nag, A. $CsPbBr_3$/ZnS Core/Shell Type Nanocrystals for Enhancing Luminescence Lifetime and Water Stability. *ACS Energy Lett.* **2020**, *5* (6), 1794−1796.

(18) Nguyen, T. P.; Ozturk, A.; Park, J.; Sohn, W.; Lee, T. H.; Jang, H. W.; Kim, S. Y. Facile synthesis of $CsPbBr_3$/PbSe composite clusters. *Sci. Technol. Adv. Mater.* **2018**, *19* (1), 10−17.

(19) Wang, X.-D.; Huang, Y.-H.; Liao, J.-F.; Jiang, Y.; Zhou, L.; Zhang, X.-Y.; Chen, H.-Y.; Kuang, D.-B. In situ construction of a Cs_2SnI_6 perovskite nanocrystal/SnS_2 nanosheet heterojunction with boosted interfacial charge transfer. *J. Am. Chem. Soc.* **2019**, *141* (34), 13434−13441.

(20) Xu, F.; Meng, K.; Cheng, B.; Wang, S.; Xu, J.; Yu, J. Unique S-scheme heterojunctions in self-assembled TiO_2/$CsPbBr_3$ hybrids for CO_2 photoreduction. *Nat. Commun.* **2020**, *11* (1), 1−9.

(21) Hu, H.; Wu, L.; Tan, Y.; Zhong, Q.; Chen, M.; Qiu, Y.; Yang, D.; Sun, B.; Zhang, Q.; Yin, Y. Interfacial synthesis of highly stable $CsPbX_3$/oxide Janus nanoparticles. *J. Am. Chem. Soc.* **2018**, *140* (1), 406−412.

(22) Liu, H.; Tan, Y.; Cao, M.; Hu, H.; Wu, L.; Yu, X.; Wang, L.; Sun, B.; Zhang, Q. Fabricating $CsPbX_3$-based type I and type II heterostructures by tuning the halide composition of janus $CsPbX_3$/ZrO_2 nanocrystals. *ACS Nano* **2019**, *13* (5), 5366−5374.

(23) Li, Z.-J.; Hofman, E.; Li, J.; Davis, A. H.; Tung, C.-H.; Wu, L.-Z.; Zheng, W. Photoelectrochemically Active and Environmentally Stable $CsPbBr_3$/TiO_2 Core/Shell Nanocrystals. *Adv. Funct. Mater.* **2018**, *28* (1), 1704288.

(24) Shamsi, J.; Dang, Z.; Ijaz, P.; Abdelhady, A. L.; Bertoni, G.; Moreels, I.; Manna, L. Colloidal CsX (X = Cl, Br, I) Nanocrystals and Their Transformation to $CsPbX_3$ Nanocrystals by Cation Exchange. *Chem. Mater.* **2018**, *30* (1), 79−83.

(25) Baranov, D.; Caputo, G.; Goldoni, L.; Dang, Z.; Scarfiello, R.; De Trizio, L.; Portone, A.; Fabbri, F.; Camposeo, A.; Pisignano, D.; Manna, L. Transforming colloidal Cs_4PbBr_6 nanocrystals with poly(maleic anhydride-alt-1-octadecene) into stable $CsPbBr_3$ perovskite emitters through intermediate heterostructures. *Chem. Sci.* **2020**, *11* (15), 3986−3995.

(26) Toso, S.; Baranov, D.; Manna, L. Hidden in Plain Sight: the Overlooked Influence of the Cs^+ Substructure on Transformations in

Cesium Lead Halide Nano-crystals. *ACS Energy Lett.* **2020**, *5*, 3409−3414.
(27) Zhang, X.; Lu, M.; Zhang, Y.; Wu, H.; Shen, X.; Zhang, W.; Zheng, W.; Colvin, V. L.; Yu, W. W. PbS Capped $CsPbI_3$ Nanocrystals for Efficient and Stable Light-Emitting Devices Using p-i-n Structures. *ACS Cent. Sci.* **2018**, *4* (10), 1352−1359.
(28) Wang, S.; Bi, C.; Portniagin, A.; Yuan, J.; Ning, J.; Xiao, X.; Zhang, X.; Li, Y. Y.; Kershaw, S. V.; Tian, J.; Rogach, A. L. $CsPbI_3$/PbSe Heterostructured Nanocrystals for High-Efficiency Solar Cells. *ACS Energy Lett.* **2020**, *5* (7), 2401−2410.
(29) Toso, S.; Akkerman, Q. A.; Martín-García, B.; Prato, M.; Zito, J.; Infante, I.; Dang, Z.; Moliterni, A.; Giannini, C.; Bladt, E.; Lobato, I.; Ramade, J.; Bals, S.; Buha, J.; Spirito, D.; Mugnaioli, E.; Gemmi, M.; Manna, L. Nanocrystals of Lead Chalcohalides: A Series of Kinetically Trapped Metastable Nanostructures. *J. Am. Chem. Soc.* **2020**, *142* (22), 10198−10211.
(30) Peng, L.; Dutta, A.; Xie, R.; Yang, W.; Pradhan, N. Dot-Wire-Platelet-Cube: Step Growth and Structural Transformations in $CsPbBr_3$ Perovskite Nanocrystals. *ACS Energy Lett.* **2018**, *3* (8), 2014−2020.
(31) Peng, L.; Dutta, S. K.; Mondal, D.; Hudait, B.; Shyamal, S.; Xie, R.; Mahadevan, P.; Pradhan, N. Arm Growth and Facet Modulation in Perovskite Nanocrystals. *J. Am. Chem. Soc.* **2019**, *141* (40), 16160−16168.
(32) Imran, M.; Caligiuri, V.; Wang, M.; Goldoni, L.; Prato, M.; Krahne, R.; De Trizio, L.; Manna, L. Benzoyl halides as alternative precursors for the colloidal synthesis of lead-based halide perovskite nanocrystals. *J. Am. Chem. Soc.* **2018**, *140* (7), 2656−2664.
(33) Dutta, A.; Dutta, S. K.; Das Adhikari, S.; Pradhan, N. Tuning the size of $CsPbBr_3$ nanocrystals: all at one constant temperature. *ACS Energy Lett.* **2018**, *3* (2), 329−334.
(34) De Backer, A.; Van den Bos, K.; Van den Broek, W.; Sijbers, J.; Van Aert, S. StatSTEM: an efficient approach for accurate and precise model-based quantification of atomic resolution electron microscopy images. *Ultramicroscopy* **2016**, *171*, 104−116.
(35) Grillo, V. The effect of surface strain relaxation on HAADF imaging. *Ultramicroscopy* **2009**, *109* (12), 1453−1464.
(36) Wu, K.; Liang, G.; Kong, D.; Chen, J.; Chen, Z.; Shan, X.; McBride, J. R.; Lian, T. Quasi-type II $CuInS_2$/CdS core/shell quantum dots. *Chem. Sci.* **2016**, *7* (2), 1238−1244.
(37) Sutton, R. J.; Filip, M. R.; Haghighirad, A. A.; Sakai, N.; Wenger, B.; Giustino, F.; Snaith, H. J. Cubic or orthorhombic? Revealing the crystal structure of metastable black-phase $CsPbI_3$ by theory and experiment. *ACS Energy Lett.* **2018**, *3* (8), 1787−1794.
(38) Nedelcu, G.; Protesescu, L.; Yakunin, S.; Bodnarchuk, M. I.; Grotevent, M. J.; Kovalenko, M. V. Fast anion-exchange in highly luminescent nanocrystals of cesium lead halide perovskites ($CsPbX_3$, X= Cl, Br, I). *Nano Lett.* **2015**, *15* (8), 5635−5640.
(39) Akkerman, Q. A.; D'Innocenzo, V.; Accornero, S.; Scarpellini, A.; Petrozza, A.; Prato, M.; Manna, L. Tuning the optical properties of cesium lead halide perovskite nanocrystals by anion exchange reactions. *J. Am. Chem. Soc.* **2015**, *137* (32), 10276−10281.
(40) Perdew, J. P.; Burke, K.; Ernzerhof, M. Generalized gradient approximation made simple. *Phys. Rev. Lett.* **1996**, *77* (18), 3865.
(41) Hutter, J.; Iannuzzi, M.; Schiffmann, F.; VandeVondele, J. cp2k: atomistic simulations of condensed matter systems. *Wiley Interdiscip. Rev. Comput. Mol. Sci.* **2014**, *4* (1), 15−25.
(42) Murphy, N.; Wortis, R.; Atkinson, W. Generalized inverse participation ratio as a possible measure of localization for interacting systems. *Phys. Rev. B: Condens. Matter Mater. Phys.* **2011**, *83* (18), 184206.
(43) Houtepen, A. J.; Hens, Z.; Owen, J. S.; Infante, I. On the origin of surface traps in colloidal II-VI semiconductor nanocrystals. *Chem. Mater.* **2017**, *29* (2), 752−761.

https://dx.doi.org/10.1021/jacs.0c10916
J. Am. Chem. Soc. 2021, 143, 1435−1446